

# Vertically Aligned Porous Organic Semiconductor Nanorod Array Photoanodes for Efficient Charge Utilization

Beidou Guo,<sup>†,‡,§</sup> Liangqiu Tian,<sup>†,‡,§</sup> Wenjing Xie,<sup>†,§</sup> Aisha Batool,<sup>†,‡</sup> Guancai Xie,<sup>†,‡</sup> Qin Xiang,<sup>†</sup> Saad Ullah Jan,<sup>†,‡</sup> Rajender Boddula,<sup>†</sup> and Jian Ru Gong<sup>\*,†,§</sup>

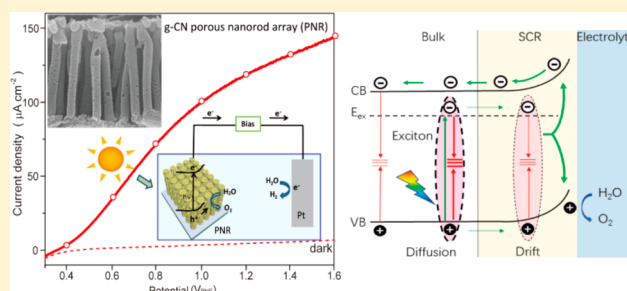
<sup>†</sup>Chinese Academy of Sciences (CAS) Key Laboratory of Nanosystem and Hierarchy Fabrication, CAS Center for Excellence in Nanoscience, National Center for Nanoscience and Technology, Beijing 100190, People's Republic of China

<sup>‡</sup>University of CAS, Beijing 100049, People's Republic of China

## Supporting Information

**ABSTRACT:** Because of inefficient charge utilization caused by localized  $\pi$ -electron conjugation and large exciton binding energy, the photoelectrochemical water-splitting efficiency of organic polymers is seriously limited. Taking the graphitic carbon nitride (g-CN) polymer as an example, we report a novel photoanode based on a vertically aligned g-CN porous nanorod (PNR) array prepared in situ, using a thermal polycondensation approach, with anodic aluminum oxide as the template. The g-CN PNR array exhibits an excellent photocurrent density of  $120.5 \mu\text{A cm}^{-2}$  at  $1.23 V_{\text{RHE}}$  under one sun illumination, the highest reported incident photon-to-current efficiency of  $\sim 15\%$  at  $360 \text{ nm}$ , and an outstanding oxygen evolution reaction stability in  $0.1 \text{ M Na}_2\text{SO}_4$  aqueous solution, which constitutes a benchmark performance among the reported g-CN-based polymer photoanodes without any sacrificial reagents. When compared with its planar counterpart, the enhanced performance of the PNR array results principally from its unique structure that enables a high degree of aromatic ring  $\pi$ -electron conjugation for higher mobility of charge carriers, provides a direct pathway for the electron transport to the substrate, produces a large portion of hole-accepting defect sites and space charge region to promote exciton dissociation, and also withstands more strain at the interface to ensure intimate contact with the substrate. This work opens a new avenue to develop nanostructured organic semiconductors for large-scale application of solar energy conversion devices.

**KEYWORDS:** Charge separation, graphitic carbon nitride, photoanode, porous nanorod array, solar water splitting, exciton dissociation



The efficient conversion of solar energy into clean hydrogen fuel by photoelectrolysis of water over semiconductors is an attractive option to alleviate energy crisis and to address environmental challenges.<sup>1</sup> Among the large number of semiconductors,<sup>2–5</sup> organic polymers show intriguing prospects by virtue of their rich sources, low cost, light weight, versatility of functionalization, thin-film flexibility, and ease of processing.<sup>6,7</sup> Graphitic carbon nitride (g-CN, strictly speaking, polymeric heptazine-based melon) is particularly attractive because it is constituted by environmentally friendly carbon and nitrogen elements<sup>8</sup> while having suitable band edges that straddle water redox potentials. Thus, g-CN is regarded as a promising material for large-scale application of photoelectrochemical (PEC) water splitting. Unfortunately, incomplete polymerization of g-CN prepared using bulk thermal polycondensation methods may decrease its bulk conductivity because of the smaller  $\pi$ -conjugated electronic structure.<sup>9</sup> Moreover, because of the high exciton binding energy of an organic polymer resulting from the low dielectric constant and the presence of significant electron–lattice interactions and electron correlation effects, g-CN

requires additional energy input to separate photogenerated electron–hole pairs when compared with its inorganic counterpart.<sup>10</sup>

In contrast with photocatalysis over g-CN powders,<sup>7,11,12</sup> the PEC method, which is favorable for exciton dissociation with an applied external bias, is still in an early stage due to difficulties in efficiently preparing a homogeneous film on appropriate substrates.<sup>13–16</sup> Recently, it has been reported that ensuring an intimate contact between g-CN and the substrate by in situ growth techniques for g-CN such as microcontact printing<sup>14</sup> and thermal vapor condensation (TVC)<sup>16</sup> leads to a lower charge-transfer resistance at the g-CN/substrate interface when compared with films obtained by depositing g-CN powders. TVC methods, which can be used for the deposition of uniform films on a substrate, have been adopted to fabricate both monomer-modified CN films<sup>17</sup> and surface layer/bulk

**Received:** July 5, 2018

**Revised:** July 28, 2018

**Published:** August 13, 2018

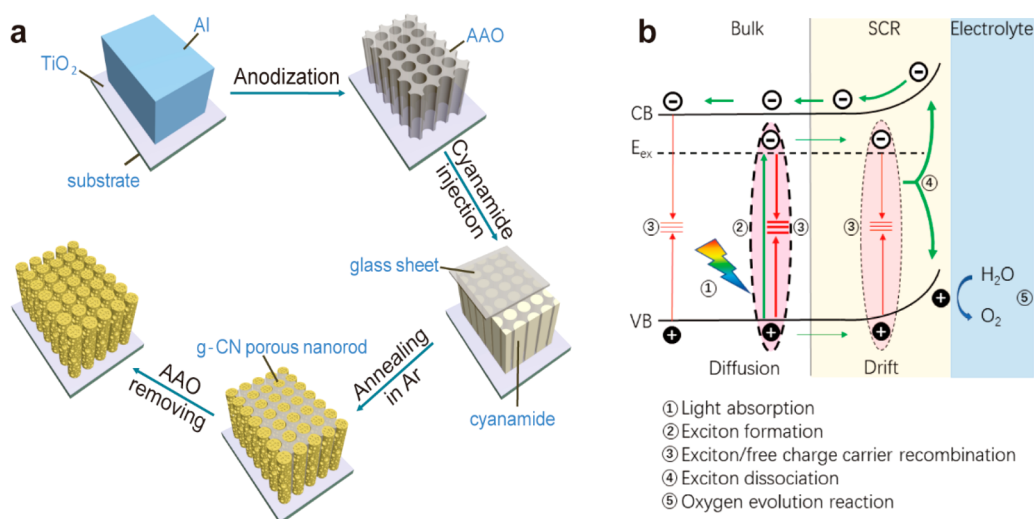


**Figure 1.** (a) Schematic procedure for fabricating a g-CN PNR array photoanode. (b) Schematic illustration of exciton dissociation and charge-transfer processes in g-CN PNR under illumination at zero bias (CB: conduction band;  $E_{\text{ex}}$ : exciton energy level; VB: valence band).

heterojunctions composed of B-doped and intrinsic CN films.<sup>18</sup> Such films have shown enhanced PEC performances owing to more efficient light absorption and higher interfacial charge separation efficiency. However, in all of the above-mentioned strategies, planar films of g-CN with a sufficiently large film thickness to ensure efficient light absorption were used. However, in a thick planar film, excitons or dissociated charges have to diffuse across relatively longer distances before reaching the surface for the redox reaction, which often results in severe bulk charge recombination.<sup>19</sup>

In this context, we report vertically aligned g-CN porous nanorod (PNR) array structure photoanodes fabricated in situ via a thermal polycondensation approach using anodic aluminum oxide (AAO) as a template (Figure 1a). In general, photoexcitation of g-CN generates excitons (coulombically bound electron–hole pairs) in the bulk at zero bias (Figure 1b). A large exciton binding energy of g-CN ( $\sim 300$  meV by theoretical calculation<sup>20</sup>) is significantly greater than the thermal energy ( $k_{\text{B}}T$ ) at room temperature.<sup>21</sup> When the exciton diffuses to the space charge region (SCR), the dissociation might occur under the high built-in electric field within SCR or at the electrode/electrolyte interface. In addition, the exciton dissociation can occur through interactions with defect sites or under the influence of an applied macroscopic electric field. Finally, the free holes transfer to the electrode surface for oxygen evolution reaction (OER), and the free electrons are collected to the back contact. During these processes, recombination of excitons and free charge carriers will also occur. Our PNR array has many advantages with respect to improving the photoanode performance over a planar g-CN bulk film: (i) The highly anisotropic 1D geometry can decouple the full absorption of light along the necessary long axis from the effective exciton diffusion over short distances in the orthogonal axis.<sup>11</sup> Moreover, the g-CN with high degree of conjugation due to the confinement effect of the template favors electron transport, and the vertically aligned 1D structure on the substrate provides a direct pathway for the transport of electrons to the substrate;<sup>22–25</sup> both of these effects lead to a higher conductivity of the g-CN array. (ii) The porous structure of PNR leads to a larger SCR with respect to the bulk<sup>26</sup> to promote exciton dissociation<sup>21</sup> and charge separation and increases the surface area to facilitate mass

transfer at the PNR/electrolyte interface.<sup>27–29</sup> (iii) The nanostructure results in a more positive valence band position, and the increased thermodynamic driving force facilitates interfacial hole transfer and OER.<sup>30</sup> (iv) Lastly, the intimate contact with the substrate resulting from in situ growth together with favorable electron transfer improves the stability of the photoanode. The nanorod array can thus withstand more strain than the planar film structure, especially when being in contact with a lattice-mismatched substrate.<sup>31</sup> In view of these features, the g-CN PNR array photoanode shows an excellent photocurrent density of  $120.5 \mu\text{A cm}^{-2}$  at 1.23 V versus reversible hydrogen electrode ( $V_{\text{RHE}}$ ) under one sun illumination, the highest incident photon-to-current efficiency of  $\sim 15\%$  at 360 nm, and an outstanding OER stability under illumination, all of which lead to a benchmark PEC performance for g-CN-based polymer photoanodes without sacrificial reagents.

The procedure for fabricating the g-CN PNR array photoanode is illustrated in Figure 1a. First, a thin film of aluminum (Al) was deposited on a fluorine-doped tin oxide (FTO) substrate covered by a thin  $\text{TiO}_2$  adhesion layer. This adhesion layer also stabilizes the anodization of the Al thin film and promotes the dissolution of the insulating alumina ( $\text{Al}_2\text{O}_3$ ) barrier layer.<sup>32–34</sup> Following Al anodization in the mixed acid electrolyte a barrier-layer-free AAO template with oriented cylindrical nanochannels was obtained (Figure S1a–c, Supporting Information). Next, the template was immersed in molten cyanamide and degassed under sonication to fill the nanochannels of AAO with cyanamide. The template with cyanamide was then annealed in a tubular furnace under an Ar atmosphere; finally, the AAO template was removed by dipping in aqueous NaOH to obtain g-CN PNR arrays with aspect ratios in the range of 8–10 on the centimeter-sized FTO substrate (Figure S1d–f, Supporting Information). In a similar manner, g-CN nanoparticle film (NPF) and bulk-film-coated photoanodes were fabricated as control samples (Figures S2 and S3; details in the Experimental Section, Supporting Information).

The cross-sectional scanning electron microscopy (SEM) image of PNR (Figure 2a) shows nanorods with an average diameter of 150 nm aligned vertically to the underlying substrate, with an intimate contact to the substrate (Figure S1f,

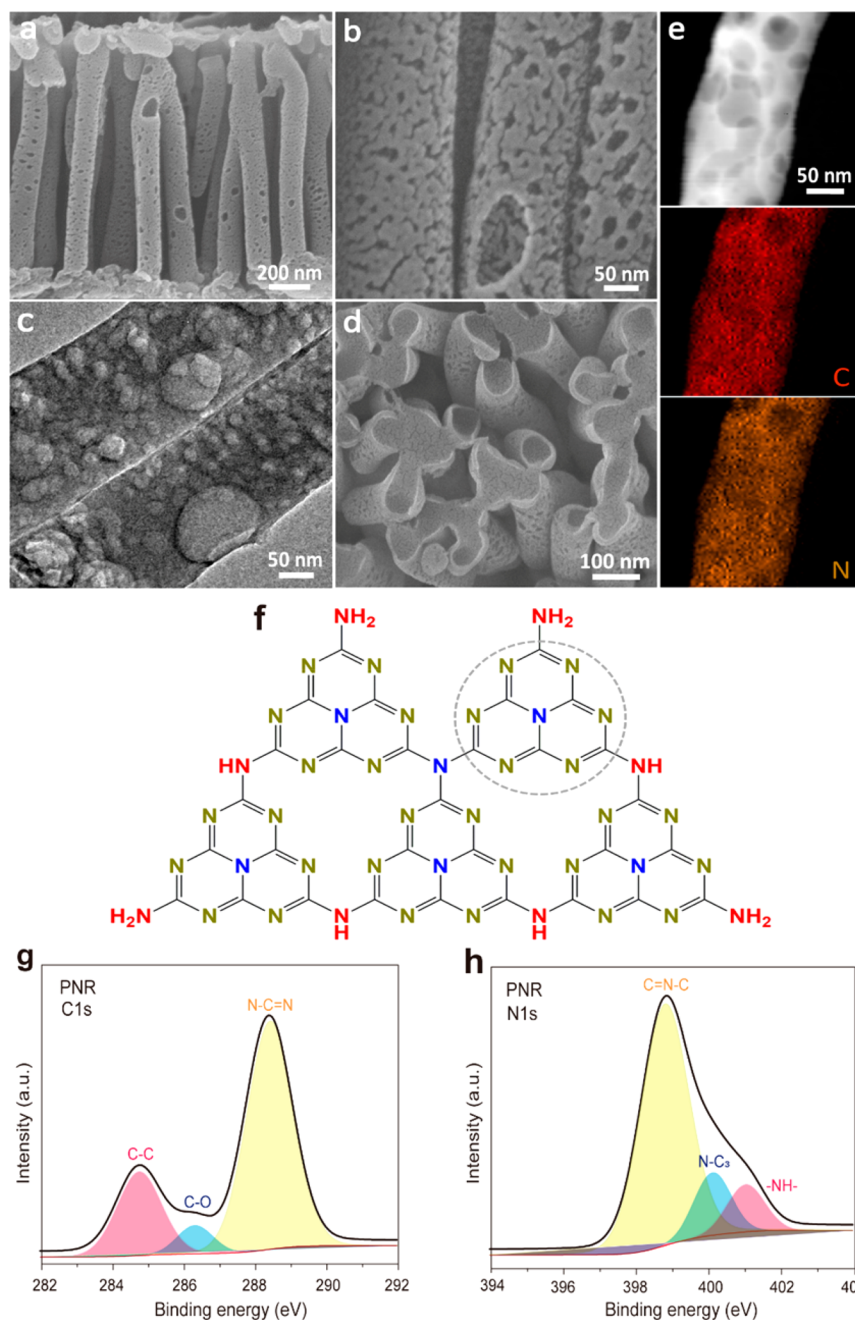


**Figure 2.** Morphology and structure characterization of the g-CN PNR photoanode. (a) Cross-sectional SEM image, (b) magnified view of the cross section, (c) high-resolution TEM image, (d) top-view SEM image, and (e) EDS carbon (red) and nitrogen (orange) elemental mapping images for g-CN PNR. (f) Schematic diagram of the typical structure of g-CN, comprising condensed heptazine repeat units with amine terminal groups (dark yellow: N in  $C=N-C$ ; blue: N in  $N-C_3$ ; red: N in  $-NH-$ ; gray circle: heptazine repeat unit of g-CN). XPS spectra of (g) C 1s and (h) N 1s of g-CN PNR.

Supporting Information). The SEM image of individual rods (Figure 2b) shows that the nanorods have a large number of pores with sizes ranging from a few to a hundred nanometers, which is further confirmed by high-resolution transmission electron microscopy (TEM, Figure 2c) and top-view SEM (Figure 2d) images. The formation of the PNR structure is due to the evaporation of a fraction of the volatile intermediate products from the AAO template. Energy-dispersive spectroscopy (EDS) elemental mapping (Figure 2e) confirms the homogeneous distribution of C and N elements throughout the PNR.

We further analyzed the chemical structures of all of the g-CN samples. The framework of g-CN is a defect-rich, N-bridged poly(heptazine) (Figure 2f). A heptazine repeat unit ( $C_6N_7$ , gray circle in Figure 2f) consists of  $N-C=N$ ,  $C=N-C$  (N in dark-yellow color, Figure 2f) and  $N-C_3$  (N in blue color, Figure 2f) structures, contributing to the  $\pi$ -conjugated electronic structures of g-CN. For  $\pi$ -conjugated polymers, the wave functions of the  $\pi$ -bands are linear combinations of the  $p_z$  orbitals from the carbon atoms in each repeat unit, and the number of sub- $\pi$ -bands is determined by the number of carbon atoms in the repeat unit of the polymer.<sup>35</sup> The interaction of these  $\pi$  electrons dictates the electronic characteristics of the



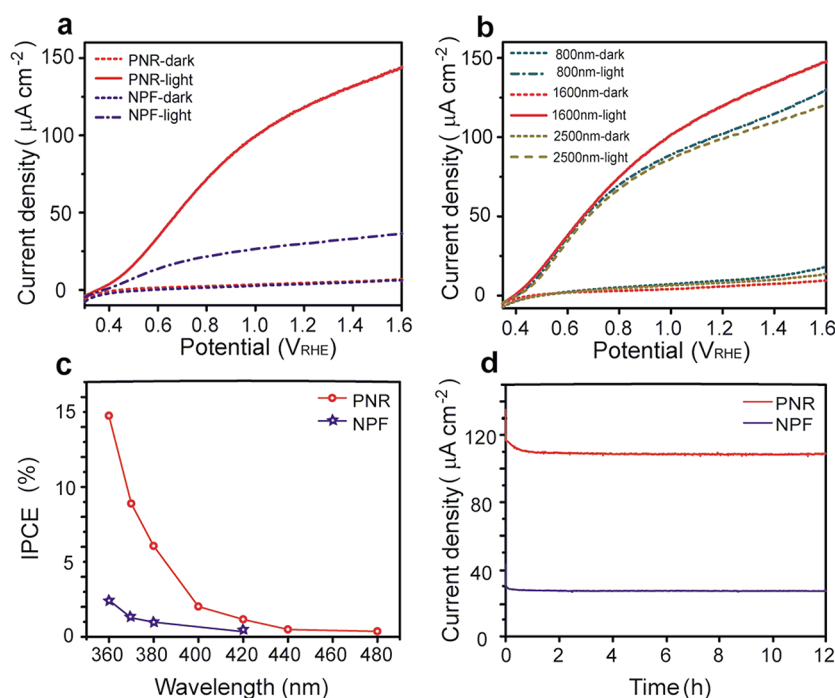


**Figure 3.** PEC performance for g-CN PNR and NPF photoanodes. (a)  $J$ - $V$  curves of g-CN PNR and NPF. (b) Height-dependent  $J$ - $V$  curves of g-CN PNR. (c) IPCE of g-CN PNR and NPF as a function of wavelength at  $1.23 \text{ V}_{\text{RHE}}$ . (d)  $I$ - $t$  curves of g-CN PNR and NPF at  $1.23 \text{ V}_{\text{RHE}}$ . All tests were carried out in  $0.1 \text{ M Na}_2\text{SO}_4$  solution (pH 5.95).

polymer. In contrast, the  $-\text{NH}-$  groups (N in red color, Figure 2f) are located at the edges of g-CN and considered as the defect sites for exciton dissociation.<sup>9,36,37</sup> Because the N atoms in  $-\text{NH}-$  groups have lone-pair electrons, they can serve as hole-accepting defect sites for enhancing exciton dissociation at the atomic level, while the dissociated electrons can participate in the delocalized  $\pi$ -bands of g-CN,<sup>38</sup> providing better electron mobility and accordingly improved PEC performance.

X-ray diffraction (XRD) patterns (Figure S4a, Supporting Information) of PNR and NPF show the characteristic (002) stacking peak of the conjugated aromatic systems of g-CN. Fourier transform infrared (FTIR) spectra (Figure S4b, Supporting Information) of both PNR and NPF display out-of-plane bending vibrations of heptazine repeat units and stretching vibrations of aromatic C-N heterocycles, indicating the formation of the basic C-N heterocycle structure of g-CN.<sup>39</sup> X-ray photoelectron spectroscopy (XPS) C 1s and N 1s spectra of PNR are shown in Figure 2g,h, and Figure S5 in the Supporting Information shows the XPS survey spectrum of PNR. Both N-C=N and C=N-C bonds can be found in g-CN PNR, implying the presence of the heptazine ring, which is the basic structural unit in g-CN.<sup>15</sup> The XPS spectrum for NPF is very similar to that of PNR (Figure S6, Supporting Information), and the XPS spectrum of the g-CN bulk film also shows characteristic features corresponding to g-CN (Figure S7, Supporting Information). Taken together, it is confirmed that the chemical composition of our PNR array, as well as those of NPF and bulk film (Figures S4–S7 and Table S1, Supporting Information), is g-CN. Furthermore, the elemental analysis shows a C/N ratio of 1.00 for the g-CN bulk film, indicating that it is nitrogen-poor structure that has been attributed to the formation of regions containing amorphous  $\text{sp}^3$  carbon (see calculation details in Table S2, Supporting Information).<sup>40</sup> However, the C/N ratio of PNR

(0.74) and NPF (0.73) is very closed to the theoretical value (0.75) of  $\text{g-C}_3\text{N}_4$ ,<sup>15</sup> indicating that more complete polymeric networks and condensed structures of g-CN can be produced via the AAO template synthesis. As a result, both nanostructured g-CN samples (PNR and NPF) have lower resistance, as displayed by the smaller Nyquist plot diameter from the electrochemical impedance spectroscopy (EIS) measurements (Figure S8, Supporting Information), because they have a higher degree of polymerization for better electron transport compared with the g-CN bulk film.

Because the  $-\text{NH}-$  concentration in g-CN is related to defects and further affects the exciton dissociation, the number of  $-\text{NH}-$  groups is then calculated in all of the g-CN samples based on the XPS results. The N 1s XPS spectra of all three samples (Figure 2h; Figures S6b and S7b, Supporting Information) can be fit into three components: C=N-C, N-C<sub>3</sub>, and  $-\text{NH}-$ , which corresponds to three types of N atoms in g-CN shown in Figure 2f. The C=N-C and N-C<sub>3</sub> structures originate from the heptazine repeat units. The  $-\text{NH}-$  groups, which represent hole-accepting defect sites in g-CN, are calculated to be 11.4 and 12.5 at% for PNR and NPF, respectively; however, they only occupy 2.7 at% in g-CN bulk film (see calculation details in Table S2, Supporting Information). Taken together, the above XPS results verify the confinement effect of the template in terms of the chemical structure difference of three g-CN samples. First, the condensed structures of PNR and NPF with a high degree of aromatic ring  $\pi$ -electron conjugation were confirmed by the C/N ratio, thus enhancing the electron mobility in the system. Second, more  $-\text{NH}-$  groups were introduced in PNR and NPF compared with the g-CN bulk film, indicating that both of the nanostructured samples have more  $-\text{NH}-$  defects for promoting exciton dissociation.

The PEC performances of the samples were evaluated in a three-electrode electrochemical system under simulated AM

1.5G sunlight illumination. The electrolyte was aqueous 0.1 M  $\text{Na}_2\text{SO}_4$  (pH 5.95) without sacrificial reagents (see details in the [Experiment Section, Supporting Information](#)). The current density–potential ( $J$ – $V$ ) curves for both PNR and NPF photoanodes display that the higher current density is obtained with increasing the applied bias ([Figure 3a](#)). It indicates that dissociation of excitons to produce the fully dissociated charge carriers can be driven by the presence of an electric field, which reduces the Coulomb potential barrier in the downfield direction and thus enhances the dissociation probability. As the field strength increases, so does the dissociation probability of the exciton state.<sup>36</sup> The g-CN PNR photoanode with an optimal nanochannel height of 1600 nm ([Figure 3b](#)) affords a photocurrent density of  $120.5 \mu\text{A cm}^{-2}$  at  $1.23 V_{\text{RHE}}$ , while 30.6 and  $20.7 \mu\text{A cm}^{-2}$  are obtained for NPF ([Figure 3a](#)) and for the bulk film ([Figure S9, Supporting Information](#)), respectively, under the same conditions. Both nanostructured samples have higher performance than the g-CN bulk film owing to their larger specific surface area, that is, the larger portion of SCR to bulk for effective exciton dissociation and charge-carrier transfer. The height-dependent  $J$ – $V$  curves of g-CN PNR ([Figure 3b](#)), in a range from 800 to 2500 nm, also show that the photocurrent first increases with the increase in the PNR height owing to the larger PNR/electrolyte interfacial area but then decreases due to more charge recombination of the longest rod with overlarge interfacial area.<sup>36</sup> Accordingly, an optimal height of  $\sim 1600$  nm was obtained in this experiment, implying that the optimal interfacial area in the nanostructured g-CN must exist to balance the exciton dissociation, charge-carrier transfer, and recombination.<sup>36</sup> In contrast, the photoanodes exhibit negligible dark currents in the potential range from 0.3 to  $1.23 V_{\text{RHE}}$ , implying that the observed currents under illumination are related exclusively to photogenerated charge carriers. To investigate the photo-response of the g-CN PNR photoanode at different wavelengths, the incident photon-to-electron conversion efficiency (IPCE) measurement was carried out at  $1.23 V_{\text{RHE}}$ . The g-CN PNR anode has an excellent IPCE value of  $\sim 15\%$  at 360 nm ([Figure 3c](#)), while  $\sim 2\%$  is observed for the NPF photoanode under the same conditions. The above results indicate that the g-CN 1D structure has a much better PEC performance than the planar film fabricated from both nanoparticle and bulk films. The PEC stability of all of the samples in 0.1 M  $\text{Na}_2\text{SO}_4$  aqueous solution was tested by applying a constant bias voltage of  $1.23 V_{\text{RHE}}$ . Both PNR and NPF of g-CN remain stable even after 12 h of continuous OER operation ([Figure 3d](#)). The performance of the bulk film photoanode shows a continuous decline ([Figure S9, Supporting Information](#)), and its stability is  $< 2$  h ([Figure S10, Supporting Information](#)), indicating that our in situ grown nanostructured g-CN photoanodes have a much higher stability than bulk films.<sup>16,17</sup> Besides the polymeric nature of g-CN with sufficient flexibility of the structure, lattice-mismatched structures on the nanoscale are likely to respond elastically to dissimilar expansions under thermal stress without breaking the structure,<sup>31</sup> which favors the high stability of nanostructured g-CN. To the best of our knowledge, our g-CN PNR has a benchmark PEC performance for the g-CN based polymer photoanodes without any sacrificial reagents (see the performance comparison in [Table S3, Supporting Information](#)).

Then, we further explore the underlying reasons for the dramatically improved PEC performance of g-CN PNR photoanodes compared with NPF. The water-splitting photo-

current density of a photoanode is the product of the photon absorption rate (i.e., the maximum photocurrent density), the charge separation efficiency ( $\eta_{\text{sep}}$ ), and the charge injection efficiency ( $\eta_{\text{inj}}$ ).<sup>41</sup> So, the light absorption characteristics were first investigated. The increasing delocalization length in g-CN makes the energy levels become closely spaced, which results in a “band” structure similar to that observed in inorganic semiconductors, as displayed in the UV–visible absorption spectra ([Figure 4a](#)). The data indicate that PNR has only a

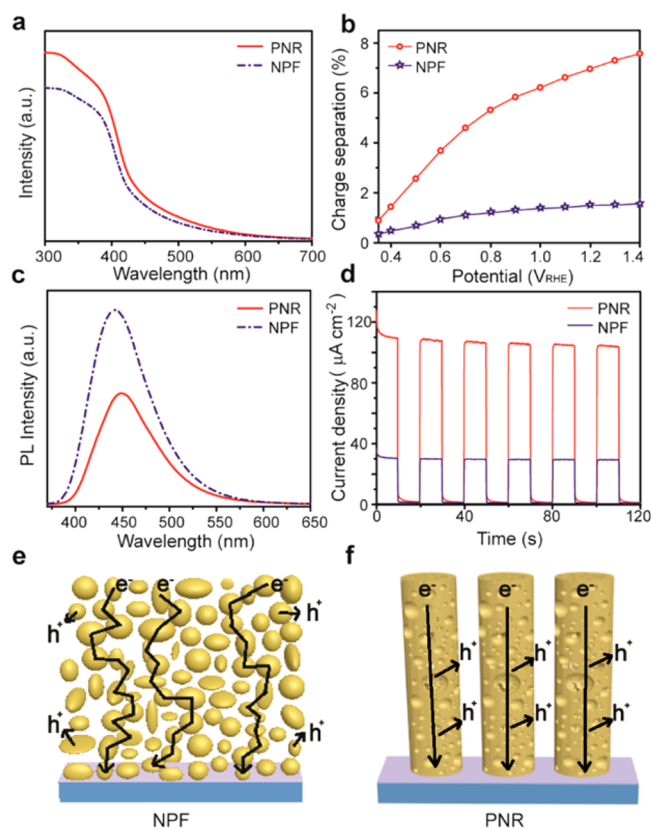


**Figure 4.** (a) UV–visible absorption spectra, (b) charge separation efficiencies, (c) PL spectra at 350 nm excitation, and (d) transient photocurrent density curves of g-CN PNR and NPF. Schematic diagrams showing the transport pathway of electrons in (e) NPF and (f) PNR of g-CN.

slightly higher light absorption intensity than NPF, which originates from the light-trapping effect of the nanorod array.<sup>42,43</sup> The maximum photocurrent density of g-CN PNR is  $1.89 \text{ mA cm}^{-2}$  (Tauc plots, [Figure S11, Supporting Information](#)), which is 1.15 times the magnitude of NPF ( $1.64 \text{ mA cm}^{-2}$ ), indicating that the slightly increased light absorption of PNR compared with NPF cannot be the main reason for its excellent PEC performance.

To investigate the behavior of photogenerated charge carriers, we introduced a hole scavenger with an extremely high rate of oxidation, into the electrolyte.<sup>4</sup> The hole scavenger  $\text{Na}_2\text{SO}_3$  serves to greatly reduce surface recombination, which allows us to calculate the efficiencies of charge injection and separation ( $\eta_{\text{inj}}$  and  $\eta_{\text{sep}}$ ) of the photoanodes ([Figure S12, Supporting Information](#)).<sup>41,44</sup> Both nanostructured g-CN samples have a high  $\eta_{\text{inj}}$  value of  $\sim 93\%$  at a potential of  $1.23 V_{\text{RHE}}$  due to their similar specific surface area (data not shown) for exciton dissociation. The more positive valence band positions of both nanostructured samples ( $1.71 \text{ V}$  vs  $\text{Ag/AgCl}$ )

compared with those of the planar films (1.42 V vs Ag/AgCl)<sup>16</sup> (Figures S13 and S14, Supporting Information) indicate that our nanostructured photoanodes have a larger thermodynamic driving force for OER. However, the similar injection efficiencies of PNR and NPF means that the difference in the PEC performance between PNR and NPF is not due to the hole injection efficiency.

Figure 4b shows a plot of the calculated  $\eta_{\text{sep}}$  as a function of the applied bias voltage for both PNR and NPF photoanodes. It is seen that PNR has a significantly higher  $\eta_{\text{sep}}$  than NPF in the whole potential range tested; for example, it is over four times that of NPF at 1.23  $V_{\text{RHE}}$ , indicating the superior charge-separation efficiency of the PNR photoanode. The separation efficiency of the photogenerated charge carriers was also qualitatively estimated from steady-state photoluminescence (PL) originating from the radiative recombination of charge carriers (Figure 4c). Compared with NPF, the lower emission peak intensity for PNR points to lower radiative recombination of the photogenerated electrons and holes, thus confirming the higher charge separation efficiency for PNR. It should be noted that no spikes are observed in the transient photocurrent curves for both PNR and NPF (Figure 4d), which further proves that efficient hole extraction occurs at the g-CN/electrolyte interface, suppressing surface recombination and photocorrosion. When compared with NPF, the improved performance of the PNR photoanode can be primarily attributed to the greatly enhanced charge separation in the photoanode. For NPF, the electron transport is characterized by slow diffusion through interparticle pathways to reach the charge collector, in a manner similar to a 3D random walk, across the nanoparticle network (Figure 4e). In this process, thermally activated hopping of electrons via multiple trapping and detrapping events can occur at the interparticle boundaries, which increase the probability of charge recombination and back reactions.<sup>22,25</sup> In contrast, the vertical 1D structure of the PNR array with decreased interfacial boundaries is beneficial to the smooth migration of electrons to the back contact (Figure 4f), accelerating electron transport and thus lowering the recombination probability of charge carriers. Hence, besides the confinement effect of the AAO template previously mentioned, the 1D nature of PNR also helps to improve its conductivity. This conclusion is further validated by the smaller Nyquist plot diameter of PNR in EIS plots (Figure S8, Supporting Information) compared with that for NPF.

In conclusion, the novel vertically aligned g-CN PNR array photoanode has been successfully prepared in situ by thermal polycondensation using AAO as the template. The PNR array anode exhibits an excellent photocurrent density of 120.5  $\mu\text{A cm}^{-2}$  at 1.23  $V_{\text{RHE}}$  under one sun illumination, the highest IPCE of  $\sim 15\%$  at 360 nm, and an outstanding OER stability, leading to a benchmark PEC performance for g-CN based polymer photoanodes without any sacrificial reagents. The macroscopic electric field applied by the PEC method promotes the exciton dissociation in both bulk and nanostructured g-CN films. Compared with its planar bulk counterpart, the nanostructured g-CN enables a high degree of aromatic ring  $\pi$ -electron conjugation to improve the mobility of charge carriers and produces a large portion of hole-accepting defect sites and SCR to promote exciton dissociation via the template confinement and also improves the electrode stability by the in situ film growth. Compared with NPF, the 1D morphology of PNR greatly expedites the

electron transport to the back contact electrode. Further improvement in PNR performance is expected by bringing together different strategies such as tuning composition, forming heterojunctions, or adding electrocatalysts to further enhance light absorption and charge utilization efficiency. This work opens a new avenue to develop nanostructured organic semiconductors for large-scale application of solar energy conversion devices.

## ■ ASSOCIATED CONTENT

### Supporting Information

The Supporting Information is available free of charge on the ACS Publications website at DOI: 10.1021/acs.nanolett.8b02740.

Experimental details, fabrication of photoanodes, characterizations, PEC measurements, SEM and TEM images, XRD patterns, FTIR spectra, XPS spectra and survey spectra, the attributions of deconvolution peaks, Nyquist plot,  $J$ - $V$  curves,  $I$ - $t$  curve, comparison list of PEC performance among g-CN photoanodes without sacrificial reagents, Tauc plots, Mott-Schottky plots, and schematic illustration of the energy band structures of photoanodes. (PDF)

## ■ AUTHOR INFORMATION

### Corresponding Author

\*E-mail: gongjr@nanoctr.cn.

### ORCID

Jian Ru Gong: 0000-0003-1512-4762

### Author Contributions

The manuscript was written through contributions of all authors. All authors have given approval to the final version of the manuscript.

### Author Contributions

<sup>§</sup>B.G., L.T., and W. X. contributed equally.

### Notes

The authors declare no competing financial interest.

## ■ ACKNOWLEDGMENTS

We acknowledge financial support for this work from the National Natural Science Foundation of China (21422303, 21573049), National Key R&D Program "nanotechnology" special focus (2016YFA0201600), Beijing Natural Science Foundation (2142036), the Knowledge Innovation Program, Youth Innovation Promotion Association, and Special Program of "One Belt One Road" of CAS. We also thank Dr. Kai Zhang for his helpful discussion.

## ■ REFERENCES

- (1) Pinaud, B. A.; Benck, J. D.; Seitz, L. C.; Forman, A. J.; Chen, Z.; Deutsch, T. G.; James, B. D.; Baum, K. N.; Baum, G. N.; Ardo, S.; Wang, H.; Miller, E.; Jaramillo, T. F. *Energy Environ. Sci.* **2013**, *6*, 1983–2002.
- (2) Fujishima, A.; Honda, K. *Nature* **1972**, *238*, 37–38.
- (3) Xie, G.; Zhang, K.; Guo, B.; Liu, Q.; Fang, L.; Gong, J. R. *Adv. Mater.* **2013**, *25*, 3820–3839.
- (4) Zhang, K.; Dong, T.; Xie, G.; Guan, L.; Guo, B.; Xiang, Q.; Dai, Y.; Tian, L.; Batool, A.; Jan, S. U.; Boddula, R.; Thebo, A. A.; Gong, J. R. *ACS Appl. Mater. Interfaces* **2017**, *9*, 42723–42733.
- (5) Guo, B.; Batool, A.; Xie, G.; Boddula, R.; Tian, L.; Jan, S. U.; Gong, J. R. *Nano Lett.* **2018**, *18*, 1516–1521.



- (6) Hendry, E.; Schins, J. M.; Candeias, L. P.; Siebbeles, L. D. A.; Bonn, M. *Phys. Rev. Lett.* **2004**, *92*, 196601.
- (7) Cao, S.; Low, J.; Yu, J.; Jaroniec, M. *Adv. Mater.* **2015**, *27*, 2150–2176.
- (8) Zheng, Y.; Lin, L.; Wang, B.; Wang, X. *Angew. Chem., Int. Ed.* **2015**, *54*, 12868–12884.
- (9) Li, X.-H.; Zhang, J.; Chen, X.; Fischer, A.; Thomas, A.; Antonietti, M.; Wang, X. *Chem. Mater.* **2011**, *23*, 4344–4348.
- (10) Giebink, N. C.; Wiederrecht, G. P.; Wasielewski, M. R.; Forrest, S. R. *Phys. Rev. B: Condens. Matter Mater. Phys.* **2011**, *83*, 195326.
- (11) Wang, X.; Maeda, K.; Thomas, A.; Takanabe, K.; Xin, G.; Carlsson, J. M.; Domen, K.; Antonietti, M. *Nat. Mater.* **2009**, *8*, 76–80.
- (12) Ong, W.; Tan, L.; Ng, Y.; Yong, S.; Chai, S. *Chem. Rev.* **2016**, *116*, 7159–7329.
- (13) Wang, X.; Maeda, K.; Chen, X.; Takanabe, K.; Domen, K.; Hou, Y.; Fu, X.; Antonietti, M. *J. Am. Chem. Soc.* **2009**, *131*, 1680–1681.
- (14) Xie, X.; Fan, X.; Huang, X.; Wang, T.; He, J. *RSC Adv.* **2016**, *6*, 9916–9922.
- (15) Liu, J.; Wang, H.; Chen, Z. P.; Moehwald, H.; Fiechter, S.; van de Krol, R.; Wen, L.; Jiang, L.; Antonietti, M. *Adv. Mater.* **2015**, *27*, 712–718.
- (16) Bian, J.; Li, Q.; Huang, C.; Li, J.; Guo, Y.; Zaw, M.; Zhang, R.-Q. *Nano Energy* **2015**, *15*, 353–361.
- (17) Bian, J.; Xi, L.; Huang, C.; Lange, K. M.; Zhang, R.-Q.; Shalom, M. *Adv. Energy Mater.* **2016**, *6*, 1600263.
- (18) Ruan, Q.; Luo, W.; Xie, J.; Wang, Y.; Liu, X.; Bai, Z.; Carmalt, C. J.; Tang, J. *Angew. Chem., Int. Ed.* **2017**, *56*, 8221–8225.
- (19) Li, Y.; Takata, T.; Cha, D.; Takanabe, K.; Minegishi, T.; Kubota, J.; Domen, K. *Adv. Mater.* **2013**, *25*, 125–131.
- (20) Melissen, S.; Le Bahers, T. L.; Steinmann, S. N.; Sautet, P. *J. Phys. Chem. C* **2015**, *119*, 25188–25196.
- (21) Hochbaum, A. I.; Yang, P. *Chem. Rev.* **2010**, *110*, 527–546.
- (22) Roy, P.; Kim, D.; Lee, K.; Spiecker, E.; Schmuki, P. *Nanoscale* **2010**, *2*, 45–59.
- (23) Kim, H. G.; Borse, P. H.; Jang, J. S.; Ahn, C. W.; Jeong, E. D.; Lee, J. S. *Adv. Mater.* **2011**, *23*, 2088–2092.
- (24) Xiao, F. X.; Miao, J.; Tao, H. B.; Hung, S. F.; Wang, H. Y.; Yang, H. B.; Chen, J.; Chen, R.; Liu, B. *Small* **2015**, *11*, 2115–2131.
- (25) Li, J.; Wu, N. *Catal. Sci. Technol.* **2015**, *5*, 1360–1384.
- (26) Li, C.; Li, A.; Luo, Z.; Zhang, J.; Chang, X.; Huang, Z.; Wang, T.; Gong, J. *Angew. Chem.* **2017**, *129*, 4214–4219.
- (27) Liu, Y.; Liang, L.; Xiao, C.; Hua, X.; Li, Z.; Pan, B.; Xie, Y. *Adv. Energy Mater.* **2016**, *6*, 1600437.
- (28) Li, Y.; Jin, R.; Xing, Y.; Li, J.; Song, S.; Liu, X.; Li, M.; Jin, R. *Adv. Energy Mater.* **2016**, *6*, 1601273.
- (29) Lu, X. F.; Gu, L. F.; Wang, J. W.; Wu, J. X.; Liao, P. Q.; Li, G. R. *Adv. Mater.* **2017**, *29*, 1604437.
- (30) Osterloh, F. E. *Chem. Soc. Rev.* **2013**, *42*, 2294–2320.
- (31) Martensson, T.; Svensson, C. P. T.; Wacaser, B. A.; Larsson, M. W.; Seifert, W.; Deppert, K.; Gustafsson, A.; Wallenberg, L. R.; Samuelson, L. *Nano Lett.* **2004**, *4*, 1987–1990.
- (32) Foong, T. R. B.; Sellinger, A.; Hu, X. *ACS Nano* **2008**, *2*, 2250–2256.
- (33) Schierhorn, M.; Boettcher, S. W.; Kraemer, S.; Stucky, G. D.; Moskovits, M. *Nano Lett.* **2009**, *9*, 3262–3267.
- (34) Sklar, G. P.; Paramguru, K.; Misra, M.; LaCombe, J. C. *Nanotechnology* **2005**, *16*, 1265–1271.
- (35) Heeger, A. J. *Chem. Soc. Rev.* **2010**, *39*, 2354–2371.
- (36) Clarke, T. M.; Durrant, J. R. *Chem. Rev.* **2010**, *110*, 6736–6767.
- (37) Meng, H.-F.; Hong, T.-M. *Phys. B* **2001**, *304*, 119–136.
- (38) Strobl, G. R. *The Physics of Polymers: Concepts for Understanding Their Structures and Behavior*; Springer-Verlag: Berlin, 2007; pp 287–301.
- (39) Lv, X.; Cao, M.; Shi, W.; Wang, M.; Shen, Y. *Carbon* **2017**, *117*, 343–350.
- (40) Holst, J. R.; Gillan, E. G. *J. Am. Chem. Soc.* **2008**, *130*, 7373–7379.
- (41) Yu, Y.; Zhang, Z.; Yin, X.; Kvit, A.; Liao, Q.; Kang, Z.; Yan, X.; Zhang, Y.; Wang, X. *Nature Energy* **2017**, *2*, 17045.
- (42) Fan, Z.; Razavi, H.; Do, J.-w.; Moriwaki, A.; Ergen, O.; Chueh, Y.-L.; Leu, P. W.; Ho, J. C.; Takahashi, T.; Reichertz, L. A.; Neale, S.; Yu, K.; Wu, M.; Ager, J. W.; Javey, A. *Nat. Mater.* **2009**, *8*, 648–653.
- (43) Garnett, E.; Yang, P. *Nano Lett.* **2010**, *10*, 1082–1087.
- (44) Kim, T. W.; Choi, K. S. *Science* **2014**, *343*, 990–994.